Limnol. Oceanogr., 49(3), 2004, 756–767

Variations in the mass-specific absorption coefficient of mineral particles suspended in water

Marcel Babin[1] *and Dariusz Stramski*
Marine Physical Laboratory, Scripps Institution of Oceanography, University of California at San Diego, La Jolla, California 92093-0238

Abstract

We examined the light-absorption properties of various samples of mineral particles suspended in water, which included pure mineral species (quartz, calcite, illite, kaolinite, and montmorillonite) and natural particulate assemblages such as desert dust originating from different locations in the Sahara. The absorption coefficient was measured in the spectral region from ultraviolet (UV) to near-infrared on particle suspensions, using a special measurement geometry that reduced the scattering error to a very small level. The concentrations of the total mass of particles in suspension, as well as the mineralogical and elemental composition of particulate samples, were also determined. For the samples of pure mineral species with negligible contamination with iron, absorption was undetectable in the visible spectral region. All of the examined natural assemblages of mixed mineral species showed a significant content of iron (5–29% by weight), and all these samples exhibited significant absorption in the UV and blue-green (400–550 nm) spectral regions. The spectral shape of absorption was similar to that determined on pure iron hydroxide suspension, with some spectral features (shoulders and changes in slope) superposed onto a general increase of absorption toward short wavelengths in the UV. The mass-specific absorption coefficient of the mineral samples, $a_m^*(\lambda)$, obtained by normalization of the absorption coefficient to the dry-mass concentration of particles, showed a significant positive correlation with Fe content. No such relationship was found for other elements present in particles. The range of $a_m^*(\lambda)$ values covered more than an order of magnitude (from <0.1 to ~ 1 m^2 g^{-1} near 400 nm), but the normalization of absorption coefficient to iron concentration led to a considerable reduction in variability among the samples. The iron-specific absorption coefficient, $a_{\mathrm{Fe}}^*(\lambda)$, varied from ~ 1 to 4 m^2 (g Fe)$^{-1}$ near 400 nm for the natural mixtures of mineral species. Although iron was a major pigmenting agent, its concentration could explain only part of variability observed in the absorption properties of mineral particles.

The application of pigment-bleaching methods, in combination with spectrophotometric measurements of marine particles retained on filters, makes it possible to determine experimentally the approximate contributions of phytoplankton and nonalgal particles to light absorption in the ocean (Doucha and Kubin 1976; Kishino et al. 1985; Tassan and Ferrari 1995). With this approach, several studies have documented the variations in the spectral absorption coefficient of nonalgal particles, $a_{\mathrm{NAP}}(\lambda)$, in various marine environments. The contribution of a_{NAP} to the total particulate absorption in the upper (photic) layer of the ocean can vary widely with location, time of year, and light wavelength. It is on the order of tens of percent in the blue spectral region and can reach nearly 100% in extreme cases (e.g., Nelson and Guarda 1995; Babin et al. 2003). The spectrum of $a_{\mathrm{NAP}}(\lambda)$ often fits an exponential function that increases toward short wavelengths (e.g., Roesler et al. 1989; Bricaud and Stramski 1990), similarly to colored dissolved organic matter (Bricaud et al. 1981).

In open ocean, it is generally assumed that the optical properties of nonalgal particles are dominated by organic detritus and living particles, such as bacteria, other heterotrophic organisms, and viruses (Morel and Ahn 1991; Stramski and Kiefer 1991). The contribution of mineral particles is poorly known. It has long been recognized, however, that the atmospheric transport and deposition of mineral dust originating from arid and semiarid regions such as Sahara and Asian deserts cover a large part of the global ocean (e.g., Prospero 1990) and that this represents a significant source of iron for the upper water column (Moore et al. 2002). This source of minerogenic particles has been of major interest to studies of the vertical particle fluxes to the deep ocean (e.g., Kremling and Streu 1993). In addition, some inorganic particles such as calcium carbonate liths from coccolithophores (Balch et al. 1999) and, less frequently, sulfur particles (Weeks et al. 2002), can be formed by biological activity in open ocean.

In coastal waters, mineral particles obviously represent a significant fraction of suspended particulate matter, which is related primarily to river discharge of sediments, coastal erosion by wave and current action, and bottom resuspension. In the polar seas, the release of ice-rafted particulate material also represents a source of minerogenic particles. Global river discharge is by far the most important single source of mineral particles entering the marine environment (Holeman

[1] Current address: Laboratoire d'Océanographie de Villefranche, CNRS/UPMC, B.P. 8, 06238 Villefranche-sur-Mer Cedex, France.

Acknowledgments

We are grateful to C. Guieu of Laboratoire d'Océanographie de Villefranche, for providing soil samples from Africa and Kuwait; C. MacIsaac of the Scripps Institution of Oceanography, for performing the ICP-OES analysis; J. Yang of the Lincoln University, Missouri, for the XRD analysis; and L. Ross of the Electron Beam Analytical Facility, University of Missouri, for electron beam microanalysis of the samples. The analysis of particulate organic carbon was done at Marine Science Institute Analytical Laboratory, University of California at Santa Barbara.

This study was funded by ONR Environmental Optics Program (grant N00014-98-1-0003) in U.S.A. and Centre National de la Recherche Scientifique in France.

Table 1. Description and origin of particle samples analyzed in the study.

No.	ID	Description	Origin
1	ILL	Illite	Source Clay Minerals Repository, University of Missouri (ref. no. IMt-1)
2	ILSM	Illite-smectite	Source Clay Minerals Repository, University of Missouri (ref. no. ISMt-2)
3	MON	Ca-montmorillonite	Source Clay Minerals Repository, University of Missouri (ref. no. SAz-1)
4	KAO1	Kaolinite (poorly crystallized)	Source Clay Minerals Repository, University of Missouri (ref. no. KGa-2)
5	KAO2	Kaolinite (well crystallized)	Source Clay Minerals Repository, University of Missouri (ref. no. KGa-1B)
6	CAL	Calcite	Natural crystal
7	QUA	Quartz	Natural crystal
8	SAH1	Saharan dust	Red rain, Villefranche-sur-Mer, France, Nov 1996
9	SAH2	Saharan dust	Red rain, Villefranche-sur-Mer, France, Aug 1999
10	AUS	Cliff shore particles	Palm Beach, north of Sydney, Australia
11	ICE	Ice-rafted particles	Glacier runoff, Kongsfjord, Spitsbergen
12	MOR1	Surface soil	Morocco (along the eastern border between 30° and 33°N)
13	MOR2	Surface soil	Morocco (along the eastern border between 30° and 33°N)
14	MOR3	Surface soil	Morocco (along the eastern border between 30° and 33°N)
15	MOR4	Surface soil	Morocco (along the eastern border between 30° and 33°N)
16	NIG1	Surface soil	Nigeria (southwest)
17	NIG2	Surface soil	Nigeria (southwest)
18	ALG1	Surface soil	Algeria (southeast)
19	ALG2	Surface soil	Algeria (southeast)
20	KUW	Surface soil	Kuwait (east, close to the ocean)
21	R36	Clay extract	Underground clays, Usine Mathieu, Roussillon, France
22	R37	Clay extract	Underground clays, Usine Mathieu, Roussillon, France
23	R38	Clay extract	Underground clays, Usine Mathieu, Roussillon, France
24	R39	Clay extract	Underground clays, Usine Mathieu, Roussillon, France

1968; Milliman and Syvitski 1992). Much of the river-transported material is efficiently trapped in coastal ocean on the continental shelves and slopes. Babin et al. (2003) determined the nonalgal absorption spectra, $a_{NAP}(\lambda)$, on samples collected at >300 sites located in European coastal waters. Although most of their a_{NAP} spectra showed a rather smooth exponential function increasing toward short wavelengths, some samples collected in waters where mineral particles were obviously abundant (e.g., in river plumes and resuspension zones) exhibited spectral features in the blue-green spectral region (400–550 nm) similar to those of iron oxides and oxide hydroxides (e.g., Sherman and Waite 1985).

The link between the abundance of mineral particles in seawater and light absorption can be described in terms of the mass-specific absorption coefficient of mineral particles, $a_m^*(\lambda)$. Because of the large diversity of mineral particles and the complexity of their physical and chemical properties, both the magnitude and spectral shape of $a_m^*(\lambda)$ in the ocean are expected to vary considerably. For achieving a quantitative assessment of this variability, the use of experimental approaches is necessary. To our knowledge, the only attempt to determine $a_m^*(\lambda)$ experimentally on natural marine suspensions was conducted by Bowers et al. (1996). They applied a heat treatment (500°C for 3 h) to samples from the Irish Sea to remove organic particulate matter and retain only mineral particles. After such a treatment, a_m^* at 440 nm was, on average, 0.024 $m^2\ g^{-1}$, and the $a_m^*(\lambda)$ spectra were nearly exponential, with a slope similar to that previously observed for $a_{NAP}(\lambda)$. It is uncertain, however, whether the method involving the heat treatment accurately isolates mineral particles without any adverse effect on their properties.

For the present study, we used another approach to study $a_m^*(\lambda)$. We determined $a_m^*(\lambda)$ from laboratory measurements on aqueous suspensions of several mineral species and a variety of natural mineral assemblages. We used a method that allows accurate measurements of the light-absorption spectra of particle suspensions with only a small error due to light scattering (Babin and Stramski 2002). We combined these measurements with determinations of particle mass concentration to document the variability in the magnitude and shape of the $a_m^*(\lambda)$ spectra. We also examined the elemental composition of mineral samples, to identify the most important pigmenting agents in the samples.

Materials and methods

Description of samples—We analyzed 24 samples, which included (1) pure or nearly pure mineral species, (2) natural particulate assemblages collected in different coastal environments, (3) soil samples from locations known to be sources of windblown desert dust, and (4) clays found in surface sedimentary deposits in France. Given the origins of the samples, it is reasonable to assume that they contained very small or negligible amounts of organic matter. This was verified for several samples (see below).

Our pure mineral samples consisted of common mineral species, including calcite, quartz, and the following aluminum silicate clay minerals: illite, illite-smectite, kaolinite (well and poorly crystallized), and montmorillonite (nos. 1–7 in Table 1). Calcite and quartz samples were obtained by grinding natural large crystals, and the clay minerals were obtained from the Source Clay Minerals Repository, University of Missouri.

The two Saharan dust samples (nos. 8–9 in Table 1) were collected at the Mediterranean coast in Villefranche-sur-Mer

(France) in November 1996 and August 1999 during strong red-rain events. Such events containing very high load of Saharan dust are common in this region (e.g., Chester et al. 1997). To obtain dry particulate matter, the collected samples of rainfall water were air-dried at room temperature in a covered container. The next sample (no. 10, Table 1) was reddish particulate material that had been collected at the cliff shore near Palm Beach north of Sydney (Australia) in December 2000. This shore is subject to substantial erosion caused by the action of ocean waves and nearshore currents. Sample 11 (Table 1) represents minerogenic particles derived from glacier erosion in the north polar environment. This sample was obtained from a small block of ice floating at the sea surface in Kongsfjord (western Spitsbergen) in July 1998. The sample was collected relatively close (<2 km) to the front of major glaciers, Kongsvagen and Kronebreen, where surface waters show distinct reddish color because of significant glacial discharge of meltwater and minerogenic sediments (Beszczynska-Möller et al. 1997). The pockets within the ice block contained significant amounts of particulate matter that was dark red in color. This particulate matter was air-dried at room temperature in a covered container.

Nine samples (nos. 12–20 in Table 1) were desert soils collected in the northern Africa and Kuwait. These samples were representative of sources of desert dust, primarily from the Sahara, transported via the atmosphere into the ocean (Guieu et al. 2002). All of these samples were collected in remote locations using a clean technique. The exact geographic origin and the collection and preparation protocols for samples 12–18 are described in Guieu et al. (2002). The same protocols were applied for samples 19 and 20, which were collected in the vicinity of Bou Saâda in northern Algeria and close to the ocean in Kuwait, respectively.

Finally, we analyzed four samples of ochre extracted from surface deposits located in the area of St-Amand-en-Puisay (Burgundy, France) a few kilometers from the Loire River (nos. 21–24 in Table 1). These samples were obtained from Usine Mathieu (Roussillon, France), where the pretreatment of samples by washing with water and settling by gravity led to obtaining just the smallest particles. The small grain size may therefore be representative of mineral particles found in river plumes. Ochre is of sedimentary origin, and the samples that we examined are, according to the chemical analyses performed by Usine Mathieu, composed essentially of kaolinite, quartz, and Fe-bearing minerals such as hematite and goethite. Although goethite is relatively more abundant in yellow-brown ochre (R36, R37, and R39), hematite is more abundant in red ochre (R38) (Velde 1995).

We also examined suspensions of iron hydroxide. Ferrous sulfate was dissolved in water, and a precipitate of iron hydroxide was allowed to develop during the night. Two suspensions were prepared in pure deionized water at different pH using NaOH. Additional iron hydroxide samples were prepared in seawater. Because of the buffer properties of seawater, pH remained stable at 7.9.

Absorption measurements—Before absorption measurements, the powder samples of mineral particles were suspended in pure deionized water, exposed to ultrasonication for several seconds, and then allowed to settle in a small beaker for 15–60 min, to remove large particles from the suspension. The particulate fraction that was still in suspension after the settling period was used for absorbance measurements. Iron hydroxide samples were exposed to sonication for 5–30 min before absorption measurements.

Measurements of absorption were performed using a dual-beam spectrophotometer (Lambda 18; Perkin Elmer) equipped with a 15-cm Spectralon integrating sphere (RSA-PE-18; Labsphere), as described in detail by Babin and Stramski (2002). Three replicate scans of absorbance were made from 230 to 850 nm at 1-nm intervals using a 2-nm slit. The sample filtered through a 0.2-μm filter (Acrodisc; Pall) was used as a particle-free reference. Samples and reference were put in a 1-cm quartz cuvette in a special holder (Labsphere) at the center of the integrating sphere. All measurements were made on optically thin suspensions, to avoid multiple particle-photon interactions within the cuvette. The spectral absorption coefficient of mineral particles, $a_m(\lambda)$ in m^{-1}, was calculated by multiplying the measured absorbance by ln(10) and dividing by the path length (0.01 m).

As shown by Babin and Stramski (2002), our optical setup for measuring absorption has the major advantage of providing good estimates of absorption with only a small scattering error. However, with this system, we often observed slightly negative absorbance values when absorption was null or extremely weak, which occurred in the far red and near-infrared spectral region (generally 700–800 nm) for the samples analyzed in the present study. Accordingly, all spectra were corrected by subtracting the lowest value in the near-infrared region from $a_m(\lambda)$ at all wavelengths. After this correction, very small positive values originating from instrument noise sometimes appeared at near-infrared wavelengths, where absorption was close to zero. In these cases, we report the zero values.

The effect of negative absorbance values at near-infrared wavelengths has been attributed to differences between the sample and reference measurements in terms of the fraction of incident beam reflected by cuvette walls and then escaping from the integrating sphere through the sample beam port (Babin and Stramski 2002). The negative values were obtained because more photons reflected on the second or exit wall of the cuvette (i.e., the water-glass and glass-air interfaces) escape from the sphere when measuring the particle-free (nonscattering) reference than when measuring the suspension of scattering particles. A simple way of correcting for this artifact is to shift upward the measured absorbance spectrum by a value that corresponds to the negative offset observed in the near-infrared region so that the resultant absorption values in that region are zero. As mentioned above, we applied such correction to our data, which is referred to as near-infrared null-point correction. Although this correction may be satisfactory for many natural assemblages of particles, a question remains to what extent the particles may absorb the near-infrared radiation and violate the assumption of no absorption, especially given that certain types of particles are likely to exhibit some absorption in that spectral region (Tassan and Ferrari 2003).

We conducted a special experiment to estimate an approximate level of near-infrared absorption for three samples—ICE, SAH2, and NIG2. For this estimation, we made

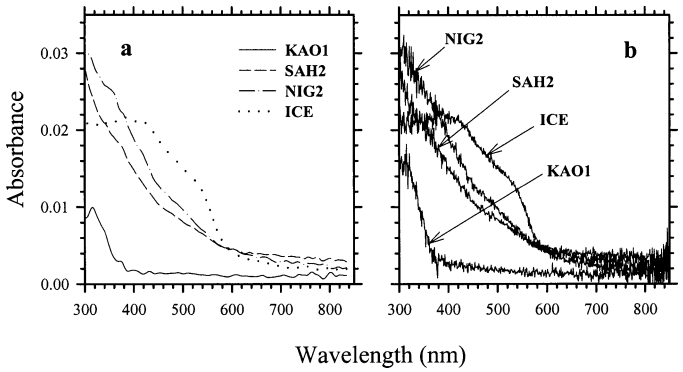

Fig. 1. Spectra of absorbance for the SAH2, NIG2, ICE, and KAO1 samples as measured with the modified 9° cuvette setup (see text for details). (a) Spectra obtained by multiple (five times) smoothing of raw absorbance data with moving average based on 7-nm intervals. Such smoothing procedure was applied to all final spectra discussed in the study. (b) Raw data with no smoothing.

measurements with a cuvette tilted by 9° in the holder inside the integrating sphere. The angle of incidence of the primary beam on the cuvette was then 9°, rather than 0°, as in the normal setup. With this modified setup, there was a negligible increase in path length (~0.6%) for the beam within the cuvette. Most important, the fraction of the primary unscattered beam after being reflected on the second wall of the cuvette did not escape from the integrating sphere through the sample beam port. This eliminated the problem of the negative absorbance values observed in the near-infrared with the normal setup. However, some scattering/reflection artifacts still existed, as suggested by small positive absorbance values observed with particle suspensions that could be assumed to have negligible absorption (such as a white powder of $MgCO_3$ suspended in water). We assumed that an approximate position of baseline representing the zero absorption in the near-infrared in our modified measurement system (9° setup) can be determined from measurements on kaolinite suspension (sample KAO1, which showed negligible absorption in the visible and near-infrared). In the determination of this baseline, the turbidity of kaolinite sample (i.e., the beam attenuation coefficient in the near-infrared as measured with the appropriately modified geometry of the spectrophotometer) was adjusted to be nearly identical at 750 nm to that of the examined ICE, SAH2, and NIG2 samples. This ensured that the scattering properties of the kaolinite sample were as close as possible to those of ICE, SAH2, and NIG2.

The results obtained with the 9° cuvette setup suggested that some samples may have sizable absorption in the near-infrared (Fig. 1). The smoothed absorption spectra for SAH2, NIG2, and ICE were significantly higher than the KAO1 spectrum in the near-infrared (Fig. 1a). Nevertheless, the magnitude of the near-infrared signal of SAH2, NIG2, and ICE above the reference level of KAO1, as expressed in the direct measurement of the absorbance values, was still very small, generally $<10^{-3}$. Such low absorbance values were below or near the level of meaningful detection with our measurement system or other similar spectrophotometers. Note that the raw (unsmoothed) spectra in the near-infrared showed a peak-to-peak amplitude of instrument noise (Fig. 1b) comparable with the differences in the ''average'' magnitude between the smoothed spectra. The low level of the possible true absorption and the instrument noise made it very difficult to accurately quantify the absorption coefficients in the near-infrared. However, to first approximation, the absorption curves in Fig. 1a suggest that the ratio of the blue–to–near-infrared absorption (400 to 800 nm) can be ~7, 18, and 31 for SAH2, NIG2, and ICE, respectively, when taking KAO1 as the baseline with zero in the near-infrared. These curves also suggest that the near-infrared null-point correction of the spectra could lead to an underestimation of absorption in the spectral region of 400–500 nm by ~14%, 6%, and 3% for SAH2, NIG2, and ICE samples, respectively. All of the spectra discussed below are presented with the null-point correction.

Dry mass, particulate organic carbon (POC), and elemental analysis—The dry mass of particles collected onto a 0.2-μm Cyclopore polycarbonate filter (Whatman) was measured using a micrometric balance (Mettler-Toledo MT5); 20 ml of sample was filtered, and the filters were dried at room temperature and low humidity (30–40%) for at least 48 h before the mass measurement. The average of triplicate measurements on different filters was used. The reproducibility (the coefficient of variation) among triplicates was always better than 5%. The absorption measurements presented below are expressed on a per unit particle dry-mass concentration, so the units for the mass-specific absorption $a_m^*(\lambda)$ are $m^2\ g^{-1}$.

The mass of POC was determined on six samples (ILL, MON, SAH1, AUS, ICE, and NIG2) by means of high-temperature combustion with a CEC 440 HA Elemental Analyzer (Control Equipment). These determinations were made on particles collected onto precombusted GF/F filters (Whatman), which were treated with 10% HCl to remove inorganic carbon and dried at 55°C before the analysis. The relative concentration of particulate organic matter was estimated by multiplying the mass of POC by a stochiometric factor of 2.6 (Copin-Montégut 1980) and dividing by the total dry mass of particles used for the POC analysis.

The elemental composition of all samples was determined with the Perkin Elmer Optima 300 XL Inductively-Coupled Plasma Optical Emission Spectrometer (ICP-OES) at the Scripps Institution of Oceanography. Thirteen elements that included most of the major crustal elements—Al, Fe, Ca, Mg, K, Ti, Ba, Sr, Zn, Mn, Ni, Cr, and V—were determined. Prior to the ICP-OES analysis, mineral samples on the filters were leached in ultrapure 1.8 N HCl in an ultrasonic bath for ~2 h, and the filters were then rinsed with distilled H_2O. The amount of sample dissolved and rinsed off the filter was determined as a difference in the dry mass of the filter before and after the treatment. The aliquot of ~400 ml of the sample solution was diluted ~12-fold with 1% HNO_3 for the ICP-OES analysis. For each sample, this analysis was performed on one or two sample filters. Several blank filters were also subjected to the same treatment and ICP-OES analysis, which showed no detectable contamination with the examined elements. Element concentrations are reported in percentages relative to the total dry weight of particles.

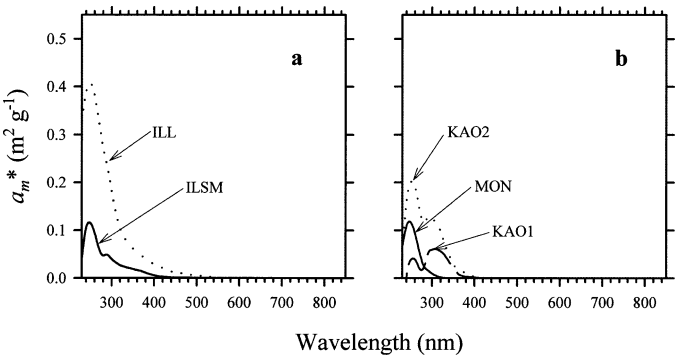

Fig. 2. Spectra of the mass-specific absorption coefficient determined on ''nearly pure'' mineral species suspended in water.

X-ray powder diffraction and X-ray microanalysis—Selected samples of natural assemblages of particles (samples SAH1 and ICE) were air-dried at room temperature, passed through a 0.25-mm sieve, and then packed in sample holders (30 mm in diameter and 2 mm in depth) for powder X-ray diffraction (XRD) analysis, to identify major mineral species present in the samples. The powdered samples were analyzed using a Scintag PADV automated, microprocessor-controlled diffractometer with Cu K_α X-ray radiation (40 kV, 30 mA) and Ge solid-state cryogenic detector. The samples were scanned within the 2–60° range of the diffraction angle 2θ, which covers the characteristic peaks of many common minerals. Mineral identification was based on matching the three strongest peaks of a given mineral species in the sample with a standard pattern of that mineral species. The XRD analysis was also made on samples 1–5, which confirmed that these samples were dominated (approximately >90–95%) by single mineral species. The illite sample (no. 4) contained small but detectable amounts of quartz. Sample 5, referred to as illite-smectite, also contained some quartz and kaolinite.

In addition to the ICP-OES and XRD analysis of the bulk samples, we examined the elemental composition of individual particles from two samples (SAH1 and ICE) with an electron-beam energy dispersive X-ray microanalysis. These samples were mounted on the scanning electron microscope (SEM) stub with double-sticky carbon tape by pressing the stub over the particles. The samples were then coated with carbon for conductivity in a vacuum evaporator. Fifty particles (>1–2 μm in size) from each sample were randomly selected for the analysis. The AMRAY 1600T SEM equipped with an energy dispersive X-ray spectrometer (EDS) was used. The EDS detector, a standard Be window model by Kevex, prohibits the analysis of elements lower than Na on the periodic table. The digital image and EDS data were collected at 20 kV accelerating voltage with the 4pi Analysis Spectral Engine system using DeskTop Spectrum Analyzer software (National Institute of Standards and Technology) for X-ray spectrum acquisition and analysis and National Institutes of Health Image software for image acquisition. In this microprobe analysis, the analytical volume of particles was estimated to range 1–4 μm^3.

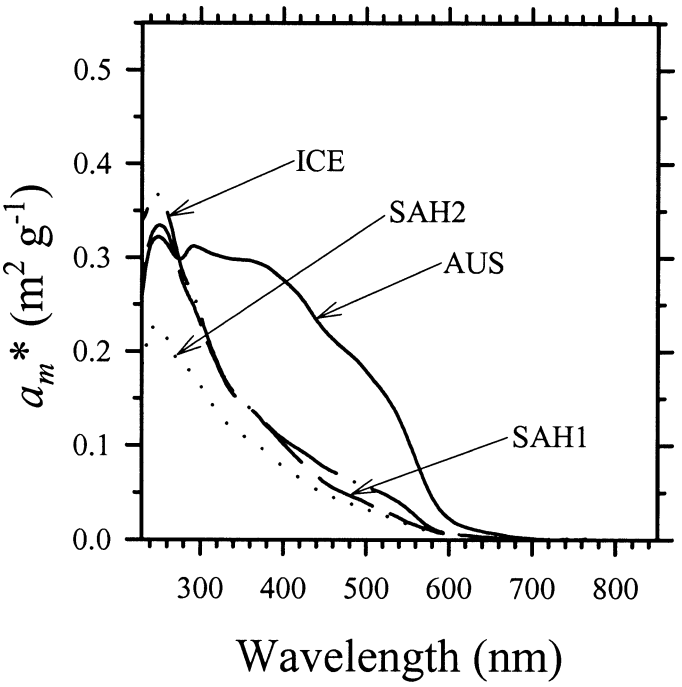

Fig. 3. Spectra of the mass-specific absorption coefficient determined on natural samples of mineral particles suspended in water. The samples were collected in coastal regions of southern France (SAH1 and SAH2), Spitsbergen (ICE), and Australia (AUS). Note that the spectral shape of the ICE sample in the visible region is significantly different from that presented in Fig. 1. These two ICE samples were prepared from two separate batches of particles collected in Kongsfjord (Spitsbergen). The observed differences in the spectral shapes of these samples indicate that significant variability in absorption properties may exist even within the same region of particle collection.

Results

The spectra of the mass-specific absorption $a_m^*(\lambda)$ are shown for all samples in Figs. 2–5. The color of the samples varied widely from white to greenish, yellowish, orange, brown, and dark red. The examined pure mineral species, except for the sample of illite, showed no detectable absorp-

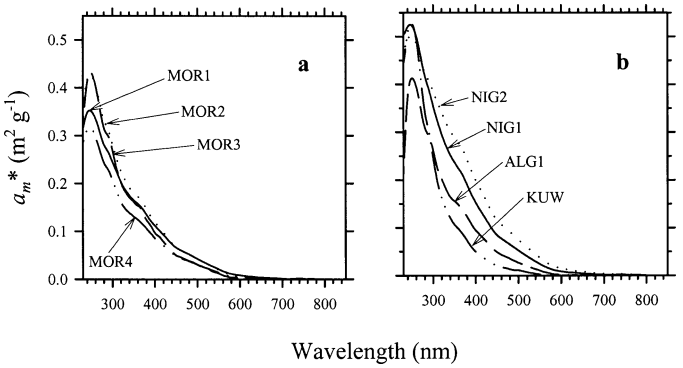

Fig. 4. Spectra of the mass-specific absorption coefficient determined on soil dust samples suspended in water. The samples were collected in the northern Africa and Kuwait.

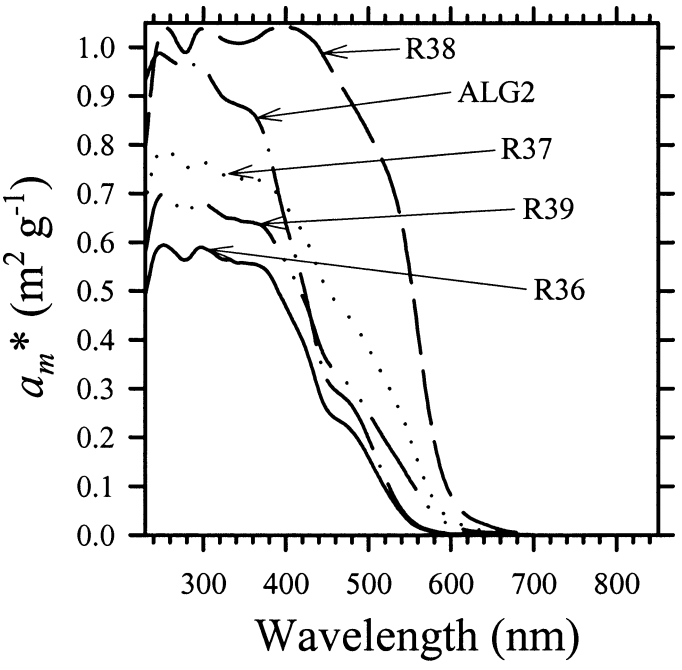

Fig. 5. Spectra of the mass-specific absorption coefficient determined on clays extracted from the underground geologic samples from the region of Roussillon (France). The absorption spectrum of the soil dust from Algeria is also included in this graph.

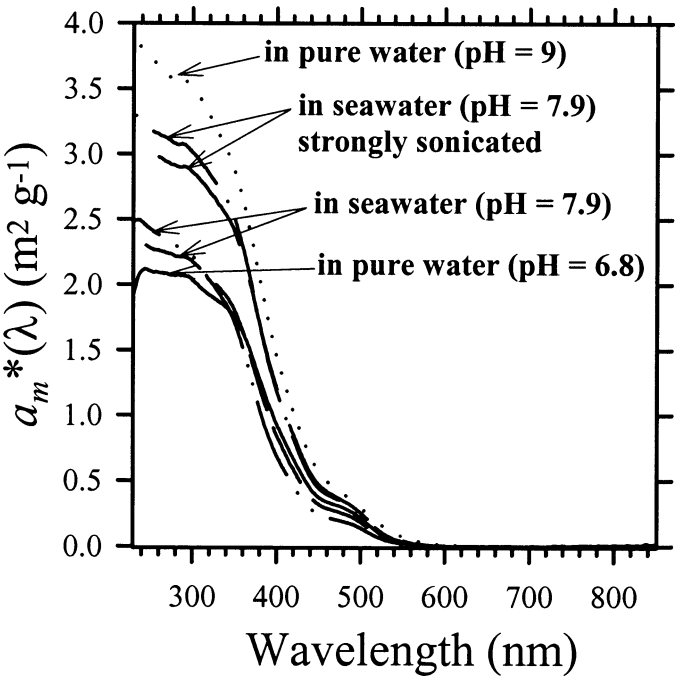

Fig. 6. Spectra of the mass-specific absorption coefficient determined on samples of iron hydroxide suspended in pure deionized water and seawater.

tion in the visible and near-infrared spectral regions (Fig. 2). Illite exhibited an increase of the absorption coefficient toward short wavelengths starting from ~500 nm. Significant absorption was observed in the near-ultraviolet (UV) for illite-smectite and kaolinite, which started to increase toward shorter wavelengths below 400 nm. The absorption coefficient of quartz and calcite was below a detectable level across the entire spectrum examined (data not shown).

The Saharan dust samples collected during red-rain events in southern France (SAH1 and SAH2) showed nearly identical absorption spectra characterized by an increase toward UV with small but discernible changes in the spectral slope in the blue-green and near-UV spectral regions (Fig. 3). The a_m^* spectrum of the ice-rafted particles from Spitsbergen (ICE) was similar in shape to the Saharan dust spectra, but the absorption magnitude was slightly higher, and the spectral shoulder in the blue-green was more pronounced and shifted toward somewhat longer wavelengths (Fig. 3). The magnitude of a_m^* for the Australian shore sample (AUS) was much larger than that of other samples shown in Fig. 3. Two broad and well-pronounced shoulders, one in the blue-green and the other in the near-UV, were superposed onto a general increase of a_m^* with decreasing wavelength. This a_m^* spectrum also showed a characteristic flattening near the value of 0.3 m^2 g^{-1} at the short-wavelength end of the spectrum.

The absorption spectra of soil dust samples collected in northern Africa (except for ALG2) and Kuwait are displayed in Fig. 4. The spectral shapes were similar among the samples and showed the same general features as those in Fig. 3: an overall increase of absorption toward the UV and more or less pronounced shoulders in the blue-green and near-UV. These features are responsible for quite obvious changes in the spectral slope—for example, near 580 and 450 nm. Although the variation in the magnitude of a_m^* for samples collected in Morocco was relatively small (Fig. 4a), a_m^* at 400 nm varied by a factor of 4 among the samples shown in Fig. 4b.

The a_m^* spectrum of the sample collected in the vicinity of Bou Saâda in northern Algeria (ALG2) is plotted in Fig. 5. The magnitude of this spectrum was significantly higher (a factor of >2) compared with other soil samples shown in Fig. 4. Figure 5 also shows the spectra of the ochre samples (R36, R37, R38, and R39), which all exhibited very high values of a_m^*. The magnitude of the R38 spectrum was the highest among the mineral particles examined. The spectral shoulders or changes in the spectral slope in the blue-green and near-UV are evident in all the curves in Fig. 5. These results also indicate that the spectral position and the extent to which these features are pronounced can vary among different mineral samples.

The a_m^* spectra measured on suspensions of iron hydroxide are displayed in Fig. 6. All spectra exhibited a similar shape with the shoulders at ~350 and 480 nm, superposed onto a general increase toward the UV. Two groups of spectra can be distinguished in terms of absorption magnitude. Higher magnitude was observed in the two iron hydroxide suspensions in seawater, which were strongly sonicated, as well as the suspension prepared in pure water at pH 9. Visual inspection of these three samples suggested that they were characterized by smaller particle size than other iron hydroxide samples exhibiting lower absorption.

The analysis of POC in six samples (ILL, MON, SAH1, AUS, ICE, and NIG2) confirmed that organic carbon constituted a small fraction, 1.5–3%, with the exception of 7%

Table 2. Elemental composition of the samples analyzed by ICP-OES. Concentrations are given in percentage of the dry mass of total particulate matter. A lack of data is indicated by a dash.

No.	ID	Al	Fe	Ca	Mg	K
1	ILL	9.68	4.43	0.21	1.34	4.43
2	ILSM	12.26	1.13	0.46	1.35	2.67
3	MON	7.12	0.84	0.89	3.57	—
4	KAO1	16.86	0.68	0.02	0.06	—
5	KAO2	12.65	0.18	0.03	0.07	—
6	CAL	0.14	0.11	33.45	0.70	—
7	QUA	0.59	—	0.21	0.21	—
8	SAH1	9.02	5.05	2.56	2.37	2.48
9	SAH2	8.95	5.10	1.12	2.19	1.83
10	AUS	9.13	16.98	0.04	0.17	2.46
11	ICE	9.99	6.28	2.81	2.54	2.88
12	MOR1	8.63	6.48	4.18	3.07	2.02
13	MOR2	9.61	5.88	1.48	2.63	2.59
14	MOR3	7.24	5.07	—	—	1.82
15	MOR4	7.59	6.92	—	—	1.28
16	NIG1	7.57	5.50	—	—	0.84
17	NIG2	9.75	5.33	—	—	0.34
18	ALG1	8.88	5.21	—	—	1.31
19	ALG2	3.91	29.05	—	—	0.42
20	KUW	4.02	3.89	—	—	—
21	R36	9.56	16.00	0.16	0.23	—
22	R37	10.33	17.42	0.11	0.24	0.84
23	R38	11.24	24.29	0.21	0.19	—
24	R39	11.16	21.74	0.13	0.22	1.25

for NIG2, of the total mass of particulate matter in these samples. These results are consistent with data that have reported low concentrations of organic matter in soil samples from Morocco, Algeria, and Nigeria (Ridame 2001).

The elemental composition obtained from ICP-OES analysis of bulk samples is given in Table 2. As expected, the concentration of Al in the clay mineral samples (nos. 1–5) was high, compared with the quartz and calcite samples (nos. 6–7) but smaller (by 21–28%) than the Al values derived from the chemical formula for these clay minerals (Lide 2001). This indicates that these samples actually contained some impurities and/or were hydrated. We note, however, that the composition of clay mineral species often varies considerably with the origin of the sample (Lide 2001). Our illite and montmorillonite samples contained K and Mg, respectively, which is consistent with their normal composition (Lide 2001). The illite sample contained, however, significant amounts of Fe (>4%). The data for KAO1 and KAO2 in Table 2 are consistent with the composition of kaolinite, whose primary elements are Si (which was not determined in the ICP-OES analysis) and Al. Although the Ca concentration of 33% measured on the calcite sample compares reasonably well with the 40% value derived from the chemical formula, the discrepancy again indicates possible impurity and/or hydration.

The significant concentrations of Al in the remaining samples that are natural mixtures of various mineral species (8–24) strongly suggest that these samples consisted largely of aluminosilicates. Iron was present in large amounts (5–29%) in all these samples. None of the other elements analyzed (Ti, Ba, Sr, Zn, Mn, Ni, Cr, and V) were present at concentrations >1%. In addition, all (or most) of these particulate assemblages probably contained significant amounts of quartz and carbonates, especially calcite. This was certainly the case for the SAH1 and ICE samples, as evidenced by data from XRD analysis and SEM-based X-ray microanalysis. The powder X-ray diffraction patterns of these samples showed major peaks associated with quartz and calcite (Fig. 7). The XRD patterns also showed the presence of kaolinite, illite, and albite. Although the XRD analysis identified a relatively small number of major mineral species present in the bulk samples, the X-ray microanalysis of individual particles revealed a large diversity in the mineral composition of the samples.

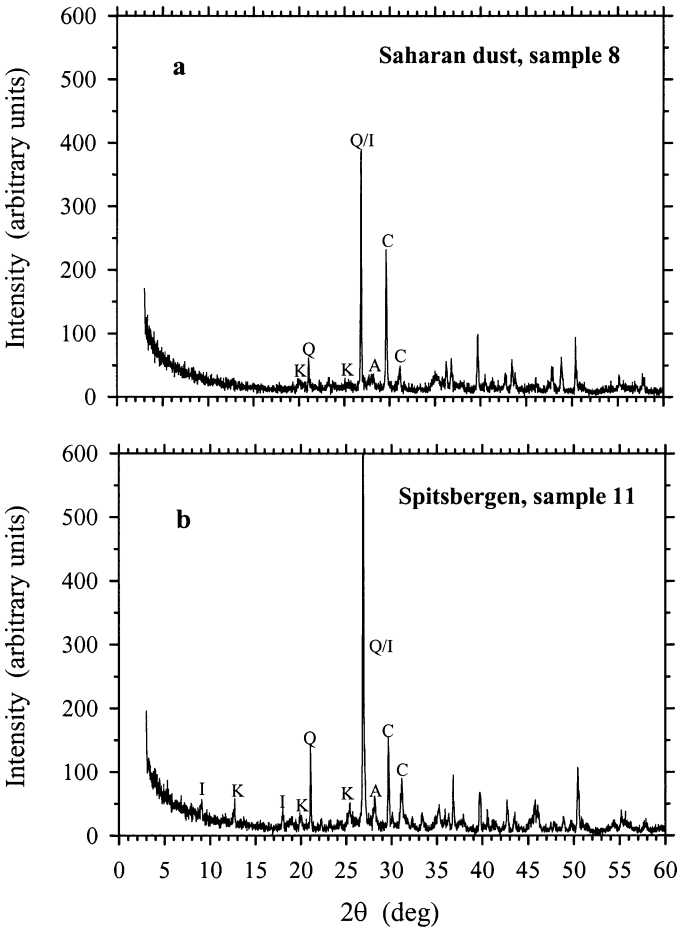

Fig. 7. Powder X-ray diffraction patterns for (a) Saharan dust, SAH1, sample 8, and (b) Spitsbergen, ICE, sample 11.

Table 3 shows the results of X-ray microanalysis for 50 particles from the SAH1 and ICE samples. Although the statistics based on 50 particles are limited, these data provide useful insights. The data confirmed that quartz (the particles containing just Si in Table 3) and carbonate minerals (the particles containing just Ca and CaMg, which correspond to calcite/aragonite and dolomite, respectively) are indeed relatively abundant in the samples. Overall, 18 and 17 of quartz and carbonate mineral grains (out of the total 50 particles) were identified in this analysis for the SAH1 and ICE samples, respectively. The remaining portion of particles could

be classified essentially as some type of aluminosilicate mineral. Apart from quartz and carbonates, we found only one additional particle in SAH1 (FeTi; ilmenite) and one particle in ICE (CaP; apatite), which are not aluminosilicates.

With regard to the aluminosilicates, Table 3 shows a wide variation in their elemental composition, which is usually difficult to use for unambiguous identification of mineral species. For example, a particle with the SiAlK composition could be illite or potash feldspar. An important result with most relevance to our study of particle absorption properties is the fact that the majority of the examined aluminosilicates contained Fe (27 and 29 particles from the SAH1 and ICE samples, respectively). Iron can generally occur either as a structural element within the mineral lattice or as a coating on particle surface. The data in Table 3 were obtained by examining the center of individual particles, but we also tested a number of particles to discover specifically whether the Fe-rich coatings can be present. In some cases, we found no Fe signature in the center of a particle (such as quartz) but detectable amounts of Fe on the particle edge, often accompanied by Al. These results suggest the presence of thin Fe oxide coatings and aluminosilicate coatings containing Fe. Of interest, no discrete iron oxide particles were identified among the 50 particles examined of the SAH1 and ICE samples. Therefore, the absorption by these samples appears to be attributable to the iron content within the different types of mineral particles rather than to discrete iron oxide and oxyhydroxide mineral grains such as hematite and goethite (see ''Discussion'' section).

Table 3. Elemental composition of 50 individual particles from the two selected samples, Saharan dust (SAH1, sample 8) and ice-rafted particles from Spitsbergen (ICE, sample 11), as determined by the X-ray microanalysis. The number of particles that exhibited the presence of a given combination of elements is shown for each sample.

Elemental composition	Saharan dust SAH1, sample 8	Spitsbergen ICE, sample 11
Si	7	12
Ca	11	3
Mg, Ca	0	2
Fe, Ti	1	0
Ca, P	0	1
Si, Al	1	1
Si, Al, K	3	2
Si, Al, K, Fe	10	16
Si, Al, K, Ti, Fe	5	0
Si, Al, K, Ca, Ti, Fe	4	0
Si, Al, Na, Fe	1	0
Si, Al, Na, K, Fe	0	1
Si, Al, Mg, Fe	0	2
Si, Al, Mg, K, Fe	1	6
Si, Al, Mg, K, Ca, Fe	5	1
Si, Al, Mg, K, Ti, Fe	1	1
Si, Al, Mg, K, Ca, Ti, Fe	0	1
Si, Al, Mg, K, Ca, Ti, Mn, Fe	0	1

Discussion

The absorption properties in the spectral region from UV to near-infrared of mineral particles present in various geologic (clays, soils, and sediments) and aerosol samples have often been studied using an approach based on diffuse reflectance spectrophotometry (Hunt and Salisbury 1970; Strens and Wood 1979; Sherman and Waite 1985; Deaton and Balsam 1991; Scheinost et al. 1998; Arimoto et al. 2002). Measurements of diffuse reflectance spectra provide a rapid and sensitive technique for the qualitative characterization of the main spectral regions of absorption and the intensity and width of the absorption bands. One important limitation of those measurements has been the lack of accurate determinations of the actual values of the spectral absorption coefficient. The absorption of minerals has also been examined on the basis of transmittance measurements on particle suspensions in water with laboratory spectrophotometers (e.g., Karickhoff and Bailey 1973; Sherman and Waite 1985). However, those measurements could not provide quantitative estimates of the absorption coefficient because of significant unknown error caused by light scattering in the measurement systems. In the present study, we determined accurate estimates of the absorption coefficient of the various mineral suspensions from a spectrophotometric method that was subjected to only a small error due to light scattering (Babin and Stramski 2002). This allowed us to derive the spectra of mass-specific absorption coefficient, which are essential to optical modeling and applications in oceanography, including optical remote sensing of ocean waters.

Origins of light absorption by mineral particles—To address the origins of light absorption by mineral particles that may commonly occur in suspension in aquatic environments, we will now discuss our results with regard to several ubiquitous mineral species and the role of iron as a pigmenting agent. Quartz and clays are quantitatively the most important nonbiogenous mineral particles in ocean sediments (Chester 1999). Clays are generally defined as mineral sheet-shaped particles whose diameters are <2 μm (Velde 1995). The most common clays in the marine environment are aluminosilicates, especially illite, montmorillonite, kaolinite, and chlorite (in decreasing order of importance). Calcite is the most important biogenous mineral in the marine environment (Chester 1999). We determined the absorption properties of all of these mineral species (except for chlorite) on nearly pure mineral samples. The absorption was undetectable for quartz and calcite at wavelengths $\lambda > 300$ nm. The clay minerals exhibited absorption in the UV, but only the illite sample contaminated with substantial amounts of iron showed measurable absorption in the visible range. These results indicate that the ''building blocks'' (aluminosilicates, silicates, and carbonates) of the mineral particles common to the marine environments generally show no absorption (or absorption too low to be assessed) in the visible range. Yet our samples of mixed assemblages of mineral species from various natural environments showed significant absorption of light at visible wavelengths. This was, for example, observed for the Saharan dust samples, despite the fact that the major bulk mineral components of these sam-

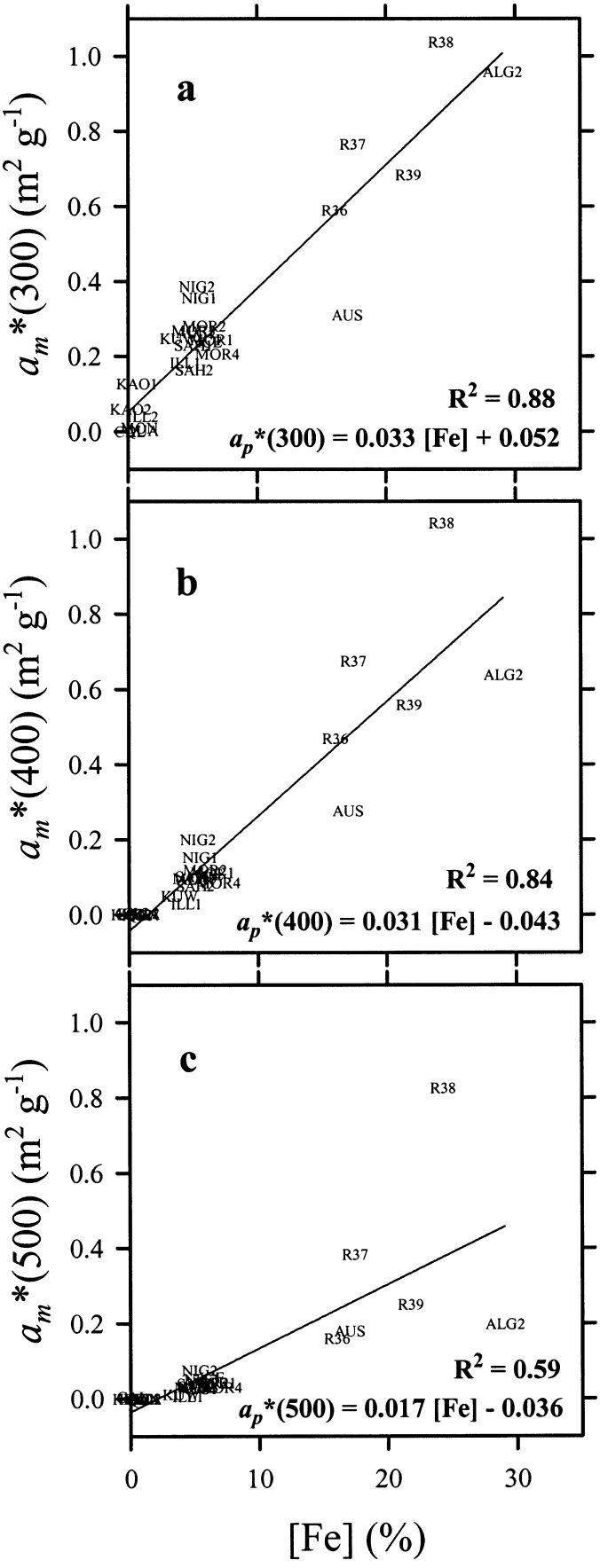

ples were illite, quartz, kaolinite, and calcite (Fig. 7, *see also* Glaccum and Prospero 1980; Avila et al. 1998).

The color of soils with a low content of organic matter has long been known to reflect iron oxide composition and content (e.g., Hunt et al. 1971; Torrent et al. 1983). Iron oxide minerals, especially hematite (Fe_2O_3) and goethite (FeOOH), can impart a red or yellowish-brown color to soils, sediments, and atmospheric dust, even if present at very small concentrations (Torrent et al. 1983; Deaton and Balsam 1991; Arimoto et al. 2002). According to Deaton and Balsam (1991), iron oxides in natural assemblages of mineral particles can be detected at concentrations as low as 0.01% by weight using diffuse reflectance spectroscopy. Using this approach, Arimoto et al. (2002) detected hematite and goethite in Saharan dust collected on islands in the North Atlantic. The relatively high concentration of Fe in our samples (5–29% by weight for samples 8–24) strongly suggests that iron was a major pigmenting agent. Figure 8 shows the correlation between $a_m^*(\lambda)$ and iron concentration in the particulate matter for these samples. The coefficient of determination was 0.88, 0.84, and 0.59 for the wavelengths of 300, 400, and 500 nm, respectively, and the intercept was close to 0. No correlation was observed between absorption and concentration of other elements (data not shown).

A few distinct types of electronic transitions that occur in Fe^{+3} minerals have been described to produce absorption in the near-UV and visible spectral regions (Karickhoff and Bailey 1973; Sherman and Waite 1985). Karickhoff and Bailey (1973) examined the absorption spectra of clay minerals that contained trace amounts of transition-metal cations and concluded that electronic transitions leading to light absorption in the UV and visible regions are associated primarily with the presence of Fe^{+3} and Fe^{+2} cations, either as structural elements within the mineral lattice or as exchangeable cations on the particle surface. Sherman and Waite (1985) further discussed the Fe^{+3} electronic transitions responsible for light absorption by iron oxides and oxide hydroxides (hematite, maghemite, goethite, and lepidocrocite). In the aquatic environment, iron can be associated with mineral particles in different ways. It can be electrostatically adsorbed on mineral particles in the form of hydroxide, it can be an element of the lattice, especially in aluminosilicates (coordination cation), and it can form crystals of oxides (e.g., hematite) and oxide hydroxides (e.g., goethite) (Velde 1995). Light absorption by such particles will mostly result from electronic transitions when (1) an electron is transferred from oxygen to iron (oxygen-metal transitions), (2) an electron is transferred between iron and an adjacent cation (intervalence charge transitions), and (3) an electron is transferred to a higher energy orbital within the same iron atom (crystal-field transitions) (Putnis 1992). Oxygen-metal tran-

←

Fig. 8. Linear regression between $a_m^*(\lambda)$ values at 300, 400, and 500 nm and the percent concentration of iron in particulate matter. The equations for the best fit and the values of squared correlation coefficient are given. The data points are shown in terms of three or four characters identifying the samples.

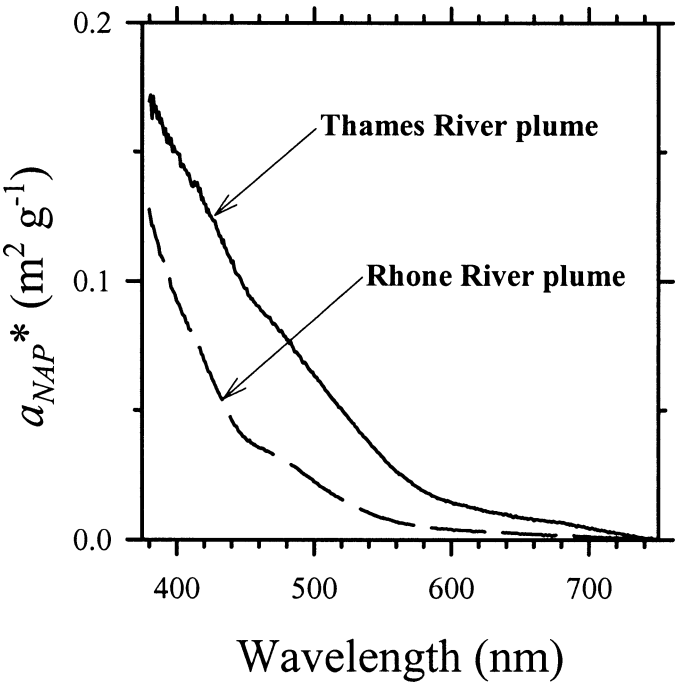

Fig. 9. Examples of mass-specific absorption spectra of nonalgal particles measured in the plumes of the Rhone River and Thames River (redrawn from fig. 13c,d in Babin et al. 2003).

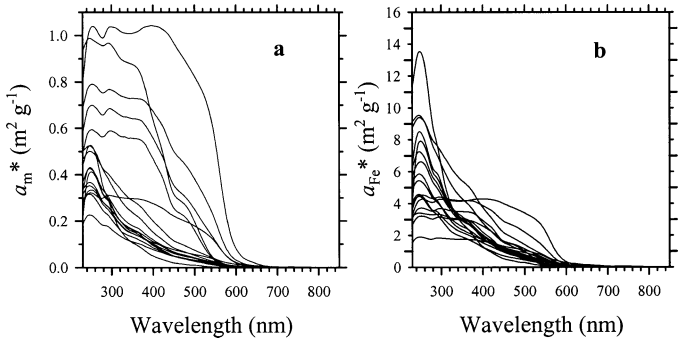

Fig. 10. Spectra of the (a) mass-specific absorption coefficient and (b) iron-specific absorption coefficient for all samples analyzed in the study, with the exception of those representing nearly pure mineral species.

sitions give rise to strong absorption in the UV (absorption edge <300 nm, where transmittance of the sample virtually drops to zero), but the associated absorption features can extend into the visible range, especially in the case of Fe^{3+}. Strong absorption bands at $\lambda > 300$ nm, including the visible wavelengths, can also be caused by intervalence transitions and the weaker features by crystal-field transitions (Putnis 1992).

The position and intensity of absorption bands related to the various types of electron transitions are highly sensitive to the local environment of iron within the lattice or at the surface of mineral particle. Nevertheless, some features in the absorption spectra that we observed appear to be typical of iron oxides. The absorption peak observed at ~250 nm for all of our samples can be attributed to oxygen → iron electron transitions that occur in octahedral and tetrahedral configurations (Karickhoff and Bailey 1973; Sherman and Waite 1985). This result is consistent with those of our elemental analysis, which showed that iron was present in all samples, including its presence in small amounts as an impurity in the samples of single mineral species. This result also supports the contention that iron can be detected in the absorption spectrum even when it is present in trace amounts (Deaton and Balsam 1991). The absorption features in the violet and blue-green spectral regions (~400–550 nm) observed in many of our samples can probably be attributed to crystal-field and intervalence transitions (Sherman and Waite 1985; Putnis 1992). The most pronounced band around 400 nm was seen for the R38 ochre sample, which contained hematite. In conclusion, the shape of absorption spectra observed in the present study strongly suggests that iron was the main pigmenting agent in our samples of mineral particles. Of interest, two examples of the nonalgal particulate absorption spectra, $a_{NAP}(\lambda)$, measured in coastal waters presumably dominated by mineral particles, displayed spectral features (shoulders and change in slope) in the visible range that resemble those associated with the presence of iron (Fig. 9). The spectral shape of these curves clearly departs from a smooth exponential-like shape often observed for the $a_{NAP}(\lambda)$ spectra dominated by organic detritus (Babin et al. 2003). When fitting an exponential function over the spectral range 350–500 nm, as described in Babin et al. (2003) to the $a_m^*(\lambda)$ spectra measured in the present study (excluding pure minerals), we obtained spectral slopes between 0.001 and 0.016 nm^{-1}. The maximum relative difference between the fit and the data in the 350–500 nm spectral range varied between 1% and 20% among samples.

Mass-specific and iron-specific absorption coefficients—The value of the mass-specific absorption coefficient a_m^* at 443 nm ranged between 0.03 and 0.1 m^2 g^{-1} for most of the natural assemblages of mineral particles analyzed (with the exception of the ochre samples). This range is consistent with the values reported for different coastal waters around Europe, where the nonalgal particulate absorption at 443 nm normalized to the dry mass of particles ranged, on average for the various regions, between 0.033 and 0.067 m^2 g^{-1} (*see* table 5 in Babin et al. 2003). For the two natural samples from the Rhone River and Thames River plumes shown in Fig. 9, which are presumably dominated by mineral particles, the mass-specific $a_{NAP}^*(443)$ was 0.044 and 0.103 m^2 g^{-1}, respectively. These values are also consistent with the range of a_m^* observed in the present study. These data indicate that a_m^* for natural assemblages of mineral particles may vary considerably (a factor >2) at visible light wavelengths, which is also supported by measurements of Asian mineral dust suspended in seawater (Stramski et al. 2004).

The variability in mineral absorption is summarized in Fig. 10, which shows all of the measurements that we made on natural (mixed) assemblages of mineral particles (samples 8–24). The absorption coefficient after normalization to the concentration of total dry mass of particles exhibited large variation, by a factor of >10 in the blue, if we consider the R38 ochre sample with the strongest absorption (Fig. 10a). However, the normalization of absorption to iron concentra-

tion leads to a significant reduction in the variability (Fig. 10b). As an example, at wavelengths near 440 nm, the iron-specific absorption coefficient, a^*_{Fe}, varied generally between 1 and 4 m^2 (g Fe)$^{-1}$. Although iron was certainly the most important pigmenting agent in the samples analyzed, significant variability remains in the $a^*_{Fe}(\lambda)$ coefficient, so iron concentration alone could explain only part of the variability in the mass-specific absorption $a^*_m(\lambda)$. The sources of unexplained variability may include changes in the form and local environment of iron occurring as a coating on particle surface or integral component of mineral grains, contributions of other transition-metal cations (e.g., titanium, manganese, and chromium), variations in the composition of particle assemblages, and the packaging effect associated with changes in particle size distribution, intraparticle concentration of pigmenting agents, or both. Recent results by Stramski et al. (2002) suggested that the package effect may indeed be a significant source of variability in $a^*_m(\lambda)$. By varying the slope of the size distribution for the same sample (SAH1, AUS, and ICE samples), they observed variations in $a^*_m(400)$ of ~10–40%, depending on the extent of a change in the size distribution.

References

ARIMOTO, R., W. L. BALSAM, AND C. SCHLOESSLIN. 2002. Visible spectroscopy of aerosol particles collected on filters: Iron-oxide minerals. Atmos. Environ. **36:** 89–96.

AVILA, A., I. QUERALT-MITJANS, AND M. ALARCON. 1998. Mineralogical composition of African dust delivered by red rains over northeastern Spain. J. Geophys. Res. **102:** 21977–21996.

BABIN, M., AND D. STRAMSKI. 2002. Light absorption by aquatic particles in the near-infrared spectral region. Limnol. Oceanogr. **47:** 911–915.

———, ———, G. M. FERRARI, H. CLAUSTRE, A. BRICAUD, G. OBOLENSKY, AND N. HOEPFFNER. 2003. Variations in the light absorption coefficients of phytoplankton, non-algal particles, and dissolved organic matter in coastal waters around Europe. J. Geophys. Res. **108:** 10.1029/2001JC000882.

BALCH, W. M., D. T. DRAPEAU, T. L. CUCCI, R. D. VAILLANCOURT, K. A. KILPATRICK, AND J. J. FRITZ. 1999. Optical backscattering by calcifying algae: Separating the contribution of particulate inorganic and organic carbon fractions. J. Geophys. Res. **104:** 1541–1558.

BESZCZYNSKA-MÖLLER, A., J. M. WESLAWSKI, W. WALCZOWSKI, AND M. ZAJACZKOWSKI. 1997. Estimation of glacial meltwater discharge into Svalbard coastal waters. Oceanologia **39:** 289–298.

BOWERS, D. G., G. E. L. HARKER, AND B. STEPHAN. 1996. Absorption spectra of inorganic particles in the Irish Sea and their relevance to remote sensing of chlorophyll. Int. J. Remote Sens. **17:** 2449–2460.

BRICAUD, A., A. MOREL, AND L. PRIEUR. 1981. Absorption by dissolved organic matter of the sea (yellow substance) in the UV and visible domains. Limnol. Oceanogr. **26:** 43–53.

———, AND D. STRAMSKI. 1990. Spectral absorption coefficients of living phytoplankton and nonalgal biogenous matter: A comparison between Peru upwelling area and the Sargasso Sea. Limnol. Oceanogr. **35:** 562–582.

CHESTER, R. 1999. Marine geochemistry, 2nd ed. Blackwell.

———, M. NIMMO, AND P. A. CORCORAN. 1997. Rain water-aerosol trace metal relationships at Cap-Ferrat: A coastal site in the Western Mediterranean. Mar. Chem. **58:** 293–312.

COPIN-MONTÉGUT, G. 1980. Matière en suspension dans les eaux de mer: Répartition, composition chimique, origine et évolution. Laboratoire de Physique et Chimie Marines, Univ. Pierre et Marie Curie.

DEATON, B. C., AND W. L. BALSAM. 1991. Visible spectroscopy—a rapid method for determining hematite and goethite concentration in geological materials. J. Sediment. Petrol. **61:** 628–632.

DOUCHA, J., AND S. KUBIN. 1976. Measurement of in vivo absorption spectra of microscopic algae using bleached cells as reference sample. Arch. Hydrobiol. Suppl. **49:** 199–213.

GLACCUM, R. A., AND J. M. PROSPERO. 1980. Saharan aerosols over the tropical North Atlantic—mineralogy. Mar. Geol. **37:** 295–321.

GUIEU, C., M.-D. LOYË-PILOT, C. RIDAME, AND C. THOMAS. 2002. Chemical characterization of the Saharan dust end-member: Some biogeochemical implications for the western Mediterranean Sea. J. Geophys. Res. **107:** 5-1–5-11.

HOLEMAN, J. N. 1968. The sediment yield of major rivers of the world. Water Resour. Res. **4:** 737–747.

HUNT, G. R., AND J. W. SALISBURY. 1970. Visible and near-infrared spectra of minerals and rocks. I. Silicate minerals. Mod. Geol. **1:** 283–300.

———, ———, AND C. J. LENHOFF. 1971. Visible and near-infrared spectra of minerals and rocks. III. Oxides and hydroxides. Mod. Geol. **2:** 195–205.

KARICKHOFF, S. W., AND G. W. BAILEY. 1973. Optical absorption spectra of clay minerals. Clays Clay Miner. **21:** 59–70.

KISHINO, M., M. TAKAHASHI, N. OKAMI, AND S. ICHIMURA. 1985. Estimation of the spectral absorption coefficients of phytoplankton in the sea. Bull. Mar. Sci. **37:** 634–642.

KREMLING, K., AND P. STREU. 1993. Saharan dust influenced trace element fluxes in deep North Atlantic subtropical waters. Deep-Sea Res. I **40:** 1155–1168.

LIDE, D. R. 2001. CRC handbook of physics and chemistry. CRC.

MILLIMAN, J. D., AND J. P. M. SYVITSKI. 1992. Geomorphic/tectonic control of sediment discharge to the ocean: The importance of small mountainous rivers. J. Geol. **100:** 520–540.

MOORE, J. K., S. C. DONEY, D. M. GLOVER, AND I. Y. FUNG. 2002. Iron cycling and nutrient-limitation patterns in surface waters of the world ocean. Deep-Sea Res. II **49:** 463–507.

MOREL, A., AND Y.-H. AHN. 1991. Optics of heterotrophic nanoflagellates and ciliates: A tentative assessment of their scattering role in oceanic waters compared to those of bacterial and algal cells. J. Mar. Res. **49:** 177–202.

NELSON, J. R., AND S. GUARDA. 1995. Particulate and dissolved spectral absorption on the continental shelf of the southeastern United States. J. Geophys. Res. **100:** 8715–8732.

PROSPERO, J. M. 1990. Mineral-aerosol transport to the North Atlantic and North Pacific: The impact of African and Asian sources, p. 59–86. *In* A. H. Knap [ed.], The long range atmospheric transport of natural and contaminant substances. Kluwer.

PUTNIS, A. 1992. Introduction to mineral sciences. Cambridge Univ. Press.

RIDAME, C. 2001. Rôle des apport atmosphériques d'origine continentale dans la biogéochimie marine: impact des apports sahariens sur la production primaire en Méditerranée. Ph.D. thesis. Univ. Paris 6 (Pierre et Marie Curie).

ROESLER, C. S., AND M. J. PERRY. 1989. Modeling in situ phytoplankton absorption from total absorption spectra in productive inland marine waters. Limnol. Oceanogr. **34:** 1510–1523.

SCHEINOST, A. C., A. CHAVERNAS, V. BARRÓN, AND J. TORRENT. 1998. Use and limitations of second-derivative diffuse reflectance spectroscopy in the visible to near-infrared range to iden-

tify and quantify Fe oxide minerals in soils. Clays Clay Miner. **46:** 528–536.

SHERMAN, D. M., AND T. D. WAITE. 1985. Electronic spectra of Fe^{3+} oxides and oxide hydroxides in the near IR to near UV. Am. Mineral. **70:** 1262–1269.

STRAMSKI, D., M. BABIN, AND S. B. WOZNIAK. 2002. Variations in the absorption coefficient of mineral particles caused by changes in the particle size distribution and refractive index. Proceedings of the XVI Ocean Optics Conference, Santa Fe, New Mexico.

———, AND D. A. KIEFER. 1991. Light scattering by microorganisms in the open ocean. Prog. Oceanogr. **28:** 343–383.

———, S. B. WOZNIAK, AND P. J. FLATAU. 2004. Optical properties of Asian mineral dust suspended in seawater. Limnol. Oceanogr. **49:** 749–755.

STRENS, R. G. J., AND B. J. WOOD. 1979. Diffuse reflectance spectra and optical properties of some iron and titanium oxides and hydroxides. Mineral. Mag. **43:** 347–354.

TASSAN, S., AND G. M. FERRARI. 1995. An alternative approach to absorption measurements of aquatic particles retained on filters. Limnol. Oceanogr. **40:** 1358–1368.

———, AND ———. 2003. Variability of light absorption by aquatic particles in the near-infrared spectral region. Appl. Opt. **42:** 4802–4810.

TORRENT, J., U. SCHWERTMANN, H. FECHTER, AND F. ALFEREZ. 1983. Quantitative relationships between soil color and hematite content. Soil Sci. **136:** 354–358.

VELDE, B. 1995. Composition and mineralogy of clay minerals, p. 8–41. *In* B. Velde [ed.], Origin and mineralogy of clays. Clays and the environment. Spinger-Verlag.

WEEKS, S. J., B. CURRIE, AND A. BAKUN. 2002. Massive emissions of toxic gas in the Atlantic. Nature **415:** 493–494.

Received: 20 May 2003
Accepted: 23 October 2003
Amended: 20 December 2003